1   A novel approach of random packing generation of complex-shaped 3D particles with controllable sizes and

2   shapes

3   Xiang Wang[1,2], Zhen-Yu Yin[2], Dong Su[1*], Xiaoxin Wu[3], Jidong Zhao[4]

4   [1] College of Civil and Transportation Engineering, Shenzhen University, Shenzhen, China.

5   Underground Polis Academy, Shenzhen University, Shenzhen, China.

6   [2] Department of Civil and Environmental Engineering, The Hong Kong Polytechnic University,

7   Hung Hom, Kowloon, Hong Kong, China.

8   [3] Department of Mathematics and Statistics, Central South University, Changsha, Hunan, China.

9   [4] Department of Civil and Environmental Engineering, Hong Kong University of Science and

10   Technology, Hong Kong, China.

11   Corresponding Author   Dong SU, Ph.D. (Professor), Email: sudong@szu.edu.cn

12

13   Xiang WANG, Ph.D.

14   Post Doctor, Email: xiang.wang@connect.polyu.hk

15   Zhen-Yu YIN, Ph.D.

16   Associate Professor, Email: zhenyu.yin@polyu.edu.hk

17   Dong SU, Ph.D. (Corresponding Author)

18   Professor, Email: sudong@szu.edu.cn

19   Xiaoxin WU, Ph.D.

20   Postgraduate, Email: 1301150334@csu.edu.cn

21   Jidong ZHAO, Ph.D.

22   Professor, Email: jzhao@ust.hk

23   A research paper submitted to

24   *Acta Geotechnica*

25   First submission: 21 July 2020

26   Second submission: 7 Dec 2020

27
28 A novel approach of random packing generation of complex-shaped 3D particles with controllable sizes and shapes

29 Xiang Wang[1,2], Zhen-Yu Yin[2], Dong Su[1*], Xiaoxin Wu[3], Jidong Zhao[4]

30 Abstract: This paper presents a novel computational-geometry-based approach to generating random

31 packing of complex-shaped 3D particles with quantitatively controlled sizes and shapes for discrete

32 modeling of granular materials. The proposed method consists of the following five essential steps: (1)

33 partitioning of the packing domain into a prescribed number of random polyhedrons with desired sizes

34 and form-scale shapes using the constrained Voronoi tessellation; (2) extraction of key points from the

35 edges and facets of each polyhedron; (3) construction of a freeform curve network in each polyhedron

36 based on Bézier curve fitting; (4) generation of solid particles with smooth, convex surfaces using the

37 biharmonic-based surface interpolation of the constructed network; and (5) creation of concavity by

38 superimposing spherical harmonic-based random noise. To ensure that the obtained shape descriptors

39 (e.g., the elongation, flatness, roundness, and convexity ratio) match the hypothesized values, an inverse

40 Monte Carlo algorithm is employed to iteratively fine-tune the control parameters during particle

41 generation. The ability of the proposed approach to generate granular particles with the desired

42 geometric properties and packing is demonstrated through several examples. This study paves a viable

43 pathway for realistic modeling of granular media pertaining to various engineering and industrial

44 processes.

45 Keywords: Complex-shaped particles; granular packing; Voronoi tessellation; Bézier curve fitting;

46 Biharmonic equation; Surface interpolation; Spherical harmonics

47

48   1 Introduction

49   The geometric and morphological properties of particles, including the size, form, corner sharpness,

50   concavity and surface roughness, play distinct important roles in affecting the macro- and micro-

51   mechanical behaviors of granular materials. This has been evidenced by numerous laboratory

52   experiments [1-7] and numerical simulations [8-11]. Microscopically, the various geometric features of

53   a particle may affect its interactions and motions with the surrounding particles in a granular assembly,

54   which collectively dictates the overall mechanical responses of the material. For example, the form

55   (elongation and flatness) and the corner sharpness (roundness) tend to affect the rolling motion of a

56   particle, while the concavity (convexity ratio) may cause interlocking at the contacts between particles.

57   To differentiate the unique effect of each individual geometric feature towards understanding of their

58   collective influence on the overall behavior of a granular assembly, numerical generation of discrete

59   particles with independent size or shape characteristics of interest appears to be a viable (if not the only)

60   option.

61   Indeed, discrete modeling of granular media has received increasing popularity across many

62   scientific and engineering fields, including chemical engineering [12-14], powder engineering [15-17]

63   and civil/geotechnical engineering [18-20]. In particular, the discrete element method (DEM) prevails

64   among many discrete modeling approaches for investigating the microscopic and macroscopic

65   behaviors of granular materials [21-23]. Within the general framework of the DEM, a variety of

66   approaches have been developed to generate particles with different geometries for DEM simulations.

67   Taking the form as an example, Ng [24] developed a DEM using elliptical particles to study the

68   mechanical behavior of idealized granular materials under 2D conditions, which was further extended

69   to 3D ellipsoid particles [25-27]. Other relevant studies include the use of elongated particles with

70   rounded caps to examine the effects of elongation [28] and spherocylindrical particles to study the

71   effects of different aspect ratios [29, 30] on granular behavior. Other studies have focused on shape

72   features other than the form. For example, superellipsoid particles [31] and superquadric particles [32]

73   have been used to simulate ellipsoid-like particles with different degrees of angular sharpness at the

74   corners in discrete element simulations. Particles with asymmetric shapes but smooth surfaces have also

75   been proposed, such as egg-shaped particles [33] and polyellipsoid particles [34]. Random simple

76   convex polyhedral particles [35] have also been proposed to simulate real particle shapes, but with

77   rather limited quantitative control of the shape features. Other recent efforts have focused on employing

78   spectrum-based methods, including the Fourier series [36] and spherical harmonics [37, 38], to generate

79   realistic particles with complex shapes. The generated shape features are statistically correlated with

80   the adopted Fourier series or spherical harmonics coefficients. However, these spectrum-based

81   approaches are not without limitations. For example, they cannot adequately and independently control

82   the corner sharpness and the concavity features. As stated in [36], real sand grains exhibit some planar

83   facets and sharp corners. These features are not reproduced well by spectrum-based methods, which

84   usually disregard the potential correlation between the phase angles of each harmonic in the frequency

85   domain and assume that the phase angles are statistically independent random variables.

86   This study presents the development of a more robust technique for grain shape reconstruction. In

87   particular, it is aimed to generate random packing of irregular-shape particles with quantitative,

88   independent control of key geometrical features, including the particle size (average radius), form

89   (elongation and flatness), corner sharpness (roundness), and concavity (convexity ratio). The proposed

4

90   algorithms are developed based on three areas of previous work by the authors: (1) the Fourier-Voronoi-

91   based packing of star-like particles [36]; (2) the spherical-harmonics-based generation of realistic sand

92   particles [37]; and (3) dense packing of convex granules based on Voronoi tessellation and cubic-

93   polynomial-curve fitting [39]. First, the constrained Voronoi tessellation is employed to partition a

94   sample domain into irregular polyhedrons, namely, the Voronoi cells. The obtained polyhedrons are

95   employed as the basic elements for the particle generation. The curve fitting technique is then extended

96   to generate 3D convex particles that are inscribed to the Voronoi cell, and the edge midpoints and facet

97   centers are extracted from each polyhedron as the key points of the particle outline. The Bézier curve

98   fitting is employed to construct a curve network that passes through the extracted key points. Next, the

99   biharmonic equation is employed to develop a unique surface interpolation algorithm to generate a solid

100   particle with a closed smooth surface that is bounded by the Bézier curve network. Finally, based on

101   the inverse operation of spherical harmonics transformation, the particle concavity features are

102   quantitatively reproduced by superimposing the amplitude-controlled harmonic series of certain

103   frequencies. To make the generated non-spherical shapes resemble the desired targets, the inverse

104   Monte Carlo approach is employed to adjust the sizes and shapes of the generated particles, so that the

105   obtained geometry statistically approximates the desired one. To further demonstrate the capability of

106   the proposed algorithms, three scenarios of granular particles packing are generated with distinctive

107   sizes and shapes that approximate the prescribed targets. The proposed work paves a pathway to further

108   DEM-based studies of individual particle shape effects of each geometrical features (e.g., form, corner

109   sharpness, concavity) on the macro- and micromechanical properties of granular materials.

110

2 Random generation of irregular particles

Random polyhedrons with irregular shapes have been performed in previous studies for simulations of granular particles [40-42]. However, the generated polyhedrons frequently exhibit unrealistic sharp corners and idealized convex surface, which fail to capture the geometric features of realistic granular particles, e.g., the corner sharpness and surface concavity. In this section, we first generate an assembly of random polyhedrons using Voronoi tessellation. Then, inside polyhedrons, we generate random complex shape particles with quantitatively controlled geometric features based on a series of computational geometry algorithms and spherical harmonics.

2.1 Polyhedron generation and key point extraction

The Voronoi tessellation has been widely used in computational geometry [43]. It is employed here to randomly generate irregular polyhedrons. Typically, a random cloud of seeding points are first generated in a given domain which is then partitioned into a number of polyhedrons accordingly. The procedure is demonstrated in Fig. 1. First, as shown in Fig. 1*a*, a cubic box with unit side length is generated as the sample domain. Then, as shown in Fig. 1*b*, 20 points are randomly distributed inside a cubic domain. Next, Delaunay triangulation is performed to identify neighboring points, as shown in Fig. 1*c*. Finally, for each point, the corresponding polyhedron (Voronoi cell) is generated, as illustrated in Fig. 1*d*. In this study, each polyhedron is isolated as an individual container. Each container will be filled with a particle and the particle will be encompassed by the facets of the polyhedron. The overall shape of the particle is expected to approximate the given polyhedron to a certain extent.
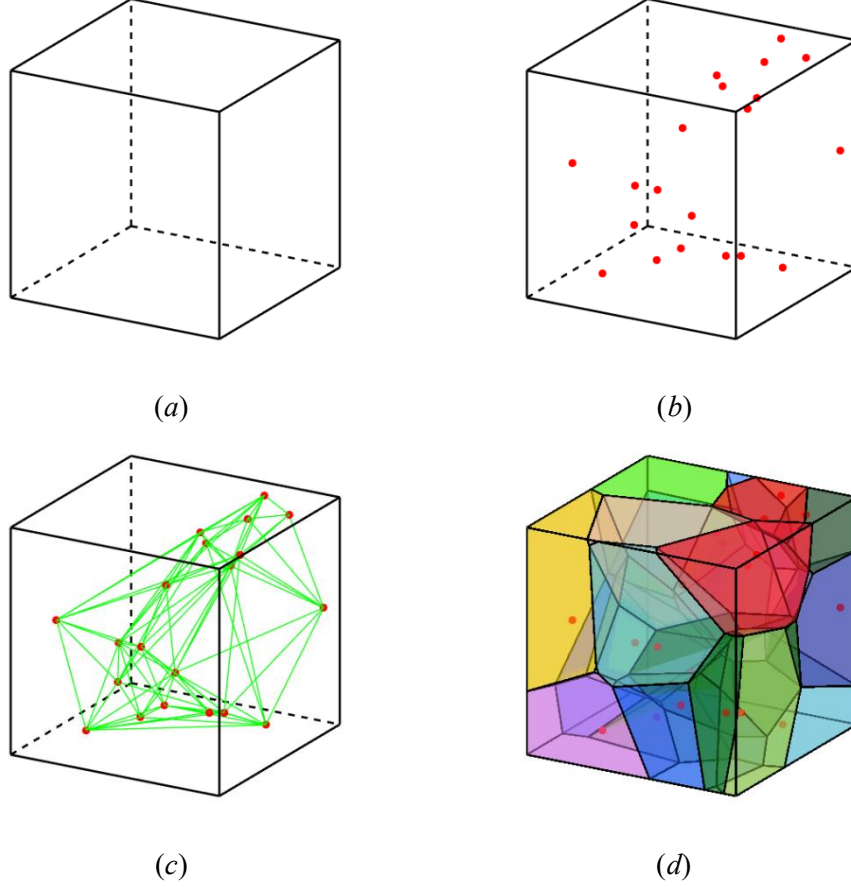
130
131   (*a*)   (*b*)

132
133   (*c*)   (*d*)

134   Fig. 1   Generation of irregular polyhedrons (*a*) define the sample domain; (*b*) node generation; (*c*)
135   Delaunay triangulation; (*d*) Voronoi tessellation

136   For each polyhedron, a series of key points are extracted from its facets and edges. An example

137   polyhedron is selected from the generated polyhedron for particle generation, as demonstrated in Fig.

138   2*a*. It is shown in Fig. 2*b* that both the midpoint (in cyan) of each side edge (in black solid line) and the

139   center point (in red) of each polyhedron facet are extracted as the key points. As illustrated in Fig. 2*c*

140   since each edge of the polyhedron is naturally shared by two neighboring facets, each edge midpoint

141   M_{edge} can be connected with two facet center points C_{facet}^{l} and C_{facet}^{R} (connected by a blue dashed

142   line). In the next section, each group of key points (one edge midpoint and the neighboring facet

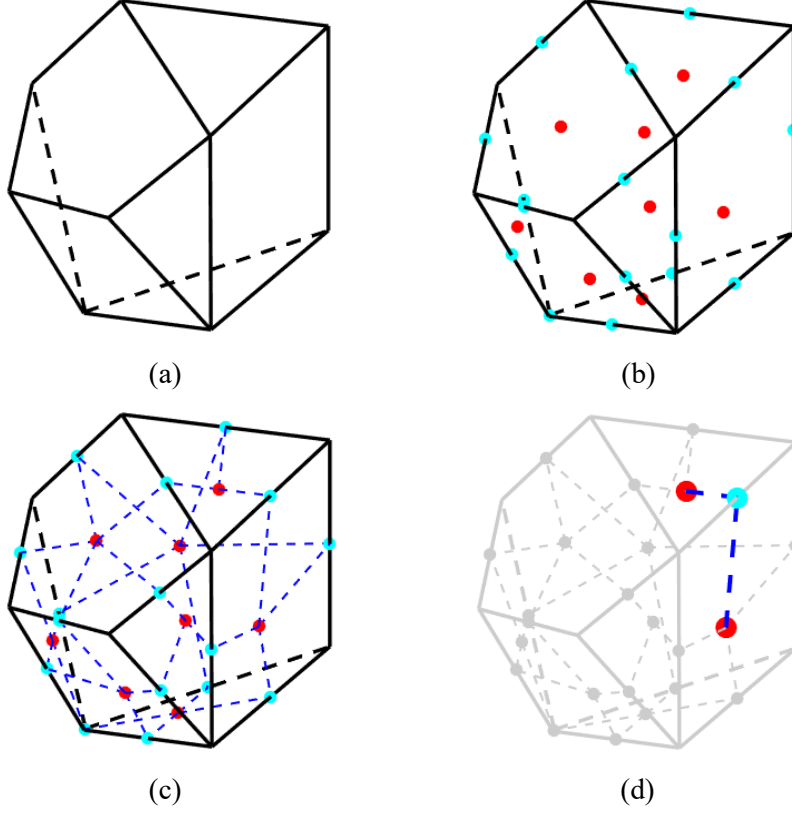143   midpoints, as highlighted in Fig. 2*d*) will be used to generate the curve network.

144

145   (a)   (b)

146

147   (c)   (d)

148   Fig. 2   Extraction of control points from the simple polyhedron

149   2.2 Generation of freeform curve network from key points

150   For an example corner $\angle C_{\text{facet}}^{l} M_{\text{edge}} C_{\text{facet}}^{R}$ (shown in Fig. 3a), which is formed by connecting an edge

151   center point M_{edge} with two neighboring facet center points C_{facet}^{l} and C_{facet}^{R}, two additional control

152   points Q_1 and Q_2 (highlighted as green points in Fig. 3b) are defined based on a curve-fitting

153   parameter w, where $w \in [0,1]$.

$$Q_1 = (1-w)C_{\text{facet}}^{l} + wM_{\text{edge}} \tag{1}$$

$$Q_2 = (1-w)C_{\text{facet}}^{R} + wM_{\text{edge}} \tag{2}$$

(a)   (b)   (c)
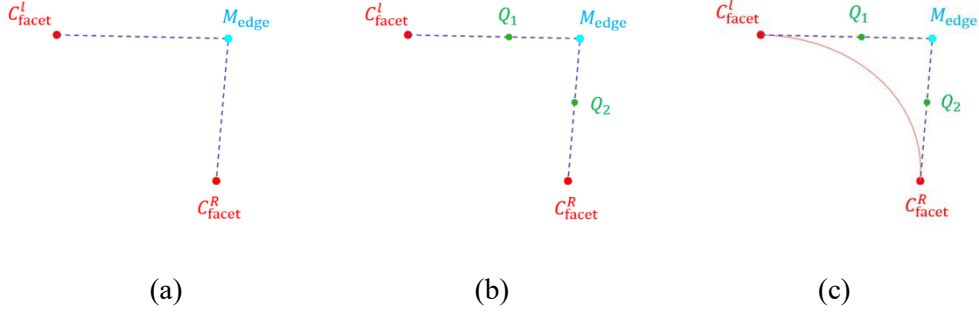
Fig. 3   Fitting the Bezier curve based on the extracted controlled points

$C_{facet}^{l}, C_{facet}^{R}, Q_1$ and Q_2 are thereby regarded as four control points to generate a cubic Bezier curve, which is tangentially oriented to lines $C_{facet}^{l}M_{edge}$ and $C_{facet}^{R}M_{edge}$ at C_{facet}^{l} and C_{facet}^{R}, respectively. The generated cubic Bezier curve (shown as a red solid curve in Fig. 3c) is expressed as follows:

$$B(u) = \sum_{i=0}^{3} B_i^3(u)P_i \tag{3}$$

where P_0 is set as C_{facet}^{l}, P_1 is set as Q_1, P_2 is set as Q_2, and P_3 is set as C_{facet}^{R}; the parametric domain of $B(u)$ is given by $u \in [0,1]$. $B_i^3(u)$ is the following cubic basis function

$$B_i^3(u) = \frac{3!}{i!\,(3-i)!} u^i (1-u)^{3-i} \tag{4}$$

The generated Bezier curves with three different shape parameter values ($w = 0.4, \ 0.6$ and 0.8) are illustrated in Fig. 4. When w increases, Q_1 and Q_2 become closer to M_{edge} but farther from C_{facet}^{l} and C_{facet}^{R}, and the generated curve more closely reflect the triangular corner $\angle C_{facet}^{l}M_{edge}C_{facet}^{R}$.

167

168   (a) $w = 0.4$ (b) $w = 0.6$ (c) $w = 0.8$
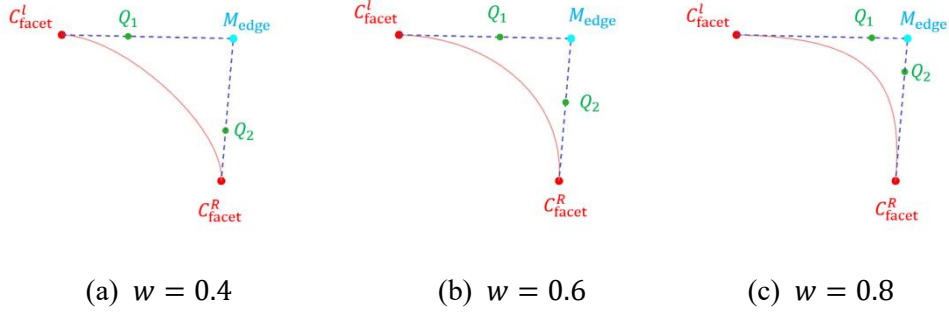
169   Fig. 4   Fitting the Bezier curve based on the extracted controlled points

170   The above Bezier curve generation process is repeated for each triangular corner of the extracted

171   key points, and finally a freeform curve network is constructed from the simple target polyhedrons, as

172   shown in Fig. 5.
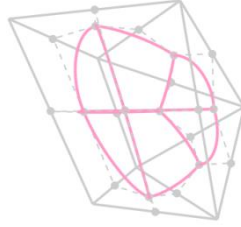

173

174   Fig. 5   Illustration of the generated freeform curve network

175   2.3 Creating the particle surface from the curve network

176   Because the terminal vertex of each curve overlaps with the facet center point of the polyhedron, the

177   generated curve network has a dual topology relation with the provided polyhedron. That is, each vertex

178   v_i (in dark blue) of the given polyhedron corresponds to a curve area CF_i, which is bounded by three

179   or four curves in the curve network. As shown in Fig. 6, one curve area CF_i in the curve network is

180   bounded by 3 curves, B_0, B_1 and B_2, which are generated from three triangular corners

181    $\angle C_{\text{facet}}^l M_{\text{edge}} C_{\text{facet}}^R$, and the edges and facets share the same vertex v_i. Based on this relation, the

182   biharmonic equation is employed to generate a curved surface for the curve area in the generated curve
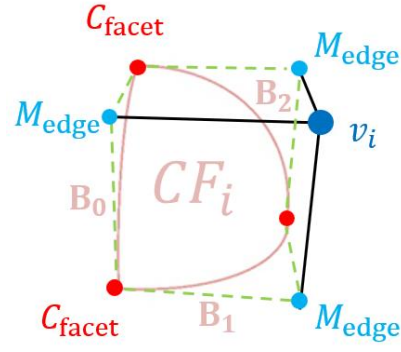
183   network.

10

Fig. 6   Curve area CF_i corresponding to vertex v_i of the given polyhedron

In this paper, we apply the biharmonic equations for smooth surface generation，which mainly focus on the generation of N-sided surface patch using biharmonic equation in the polar coordinates. The biharmonic equation fall into the category of elliptic partial differential equations (PDEs) and is commonly denoted by:

$$\Delta^2 u = 0 \tag{5}$$

where Δ^2 represents the Laplace operator and u represents either of the x, y, z dimensions. The form of the Laplace operator in polar coordinates is:

$$\Delta^2 = \left[\frac{\partial^2}{\partial r^2} + \frac{1}{r}\frac{\partial}{\partial r} + \frac{1}{r^2}\frac{\partial^2}{\partial \theta^2} \right]^2 \tag{6}$$

In this section, the equation (6) is employed as a mapping from $[0,2\pi]\times[0,1]$ to the curve area bounded by the N-sided Bezier curves. In order to solve equation (6), the boundary conditions are given by:

$$u(1,\theta) = f(\theta), \quad 0 \leq \theta \leq 1 \tag{7}$$

$$\left.\frac{\partial u}{\partial r}\right|_{r=1} = g(\theta), \quad 0 \leq \theta \leq 2\pi \tag{8}$$

11

195   where $f(\theta)$s in x, y, z dimensions describe the N-sided boundary conditions and $g(\theta)$s in x, y, z

196   dimensions control the tendency of surface generation at r direction on the boundaries, which decide

197   the normal direction n of generated surface on the boundaries by:

$$n = \left(\frac{\partial f}{\partial \theta} \times g(\theta)\right) \Big/ \left(\left|\frac{\partial f}{\partial \theta}\right| \cdot |g(\theta)|\right) \tag{9}$$

198   which can be modified through adjusting $g(\theta)$s on three dimensions to make the adjacent surfaces

199   satisfy a high continuity.

200   More specifically, the solution of (5) together with boundary conditions (7) and (8) can be obtained

201   easily and efficiently in the form as follows:

$$u(r,\theta) = \frac{a_0}{2} + \frac{b_0}{4}r^2 + \sum_{n=1}^{\infty} r^n[(a_n + c_n r^2)\cos n\theta + (b_n + d_n r^2)\sin n\theta] \tag{10}$$

202   when $f(\theta)$ and $g(\theta)$ can be expressed in the Fourier series:

$$u(1,\theta) = f(\theta), \quad 0 \le \theta \le 1 \tag{11}$$

$$\left.\frac{\partial u}{\partial r}\right|_{r=1} = g(\theta), \quad 0 \le \theta \le 2\pi \tag{12}$$

203   where α, β, δ and η can be obtained by fast Fourier transform:

$$a_n = \frac{1}{\pi}\int_0^{2\pi} f(\theta)\cos(n\theta)\,d\theta \tag{13}$$

$$\beta_n = \frac{1}{\pi}\int_0^{2\pi} f(\theta)\sin(n\theta)\,d\theta \tag{14}$$

$$\delta_n = \frac{1}{\pi}\int_0^{2\pi} g(\theta)\cos(n\theta)\,d\theta \tag{15}$$

$$\eta_n = \frac{1}{\pi} \int_0^{2\pi} g(\theta) \sin(n\theta)\, d\theta \tag{16}$$

204   or the discrete Fourier transform when the boundary conditions are given discretely as $f(\theta_i)$ and

205    $g(\theta_i)$, $i= 1, 2, 3, ..., N$ ($\theta_N=2\pi$) with the intervals denoted as s_i:

$$a_n = \frac{1}{\pi} mean[f(\theta_i) \cos(n\theta_i)\theta_i] \tag{17}$$

$$\beta_n = \frac{1}{\pi} mean[f(\theta_i) \sin(n\theta_i)\theta_i] \tag{18}$$

$$\delta_n = \frac{1}{\pi} mean[g(\theta_i) \cos(n\theta_i)\theta_i] \tag{19}$$

$$\eta_n = \frac{1}{\pi} mean[g(\theta_i) \sin(n\theta_i)\theta_i] \tag{20}$$

206   Additionally, the coefficients in equation (10) can be obtained through variable separation as

207   follows:

$$a_0 = a_0 - \frac{1}{2}\beta_0, \quad b_0 = \beta_0 \tag{21}$$

$$a_n = \frac{1}{2}[(n+2)a_n - \delta_n], \quad b_n = \frac{1}{2}[(n+2)\beta_n - \eta_n] \tag{22}$$

$$c_n = \frac{1}{2}(\delta_n - na_n), \quad d_n = \frac{1}{2}(\eta_n - n\beta_n) \tag{23}$$

208   In the actual calculation, the infinite series solution of (10) is not available, while the form of finite

209   sum is available. In order to ensure that the final surface strictly meets the boundary conditions, the

210   spectral approximation method is employed. In equation (10), r^n will decrease gradually with the

211   increase of n until it can be ignored. Using the spectral approximation technique, equation (10) can be

212   expressed as

$$u(r,\theta) = \frac{a_0}{2} + \frac{b_0}{4}r^2 + \sum_{n=1}^{M-1} r^n[(a_n + c_n r^2)\cos n\theta + (b_n + d_n r^2)\sin n\theta] + R(r,\theta) \quad (24)$$

213   where $R(r,\theta)$ is the remainder, representing the contribution of higher order terms to the solution.

214   When M is large enough, $R(r,\theta)$ can be ignored inside the surface. In order for the surface to strictly

215   meet the given boundary conditions, this item must be retained, but some approximate form is available,

216   such as

$$R(r,\theta) = A_1(\theta)r^M + A_2(\theta)r^{M+2} \qquad (25)$$

217   where $A_1(\theta)$ and $A_2(\theta)$ are pending function. For simplicity, we denote:

$$F(r,\theta) = \frac{a_0}{2} + \frac{b_0}{4}r^2 + \sum_{n=1}^{M-1} r^n[(a_n + c_n r^2)\cos n\theta + (b_n + d_n r^2)\sin n\theta]$$

$$\Delta f(\theta) = f(\theta) - F(1,\theta) \qquad (26)$$

$$\Delta g(\theta) = g(\theta) - F_r'(1,\theta)$$

218   In order to get the solution of the boundary value problem to satisfy the boundary conditions, $R(r,\theta)$

219   must satisfy the following conditions:

$$A_1(\theta) + A_2(\theta) = f(\theta) - F(1,\theta) = \Delta f(\theta) \qquad (27)$$

$$MA_1(\theta) + (M+2)A_2(\theta) = \Delta g(\theta) \qquad (28)$$

220   so we can obtain:

$$A_1(\theta) = \Delta f(\theta) - A_2(\theta) \qquad (29)$$

$$A_2(\theta) = \frac{1}{2}[\Delta g(\theta) - M\Delta f(\theta)]$$

$$(30)$$

221   Based on the above derivation, we can develop an algorithm for constructing the Biharmonic-based

222   surface as follows:

223   Table 1   Algorithm for constructing the Biharmonic-based surface

Algorithm 1
1   Compute the Fourier coefficient of the first M terms of $f(\theta)$ and $g(\theta)$ by fast Fourier transform.
2   Compute $F(1,\theta)$ and $F_r'(1,\theta)$ by equation (26)
3   Compute $A_1(\theta)$ and $A_2(\theta)$ by equations (29) and (30)
4   Compute coordinates of points on the surface by $u(r,\theta) = F(r,\theta) + R(r,\theta)$.

224   As illustrated in Fig. 7, based on the proposed algorithm, the smooth surface G that is bounded by

225   three generated Bezier curves B_0, B_1 and B_2 can be generated.

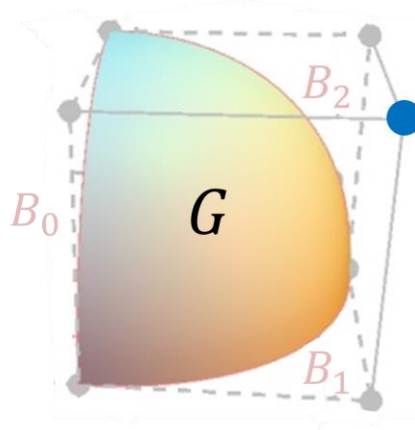226
227   Fig. 7   The generated smooth surface bounded by three Bezier curves using the proposed
228   biharmonic-equation-based method

229   The above computational process can be iterated for each curve area CF_i in the curve network

230   until a closed solid surface can be generated inside the provided polyhedron, as shown in Fig. 8a. The

231   whole procedure is repeated for each polyhedron generated by the Voronoi tessellation to produce a

232   packing of solid particles with smooth surfaces, as illustrated in Fig. 8b. Comparing with the

15

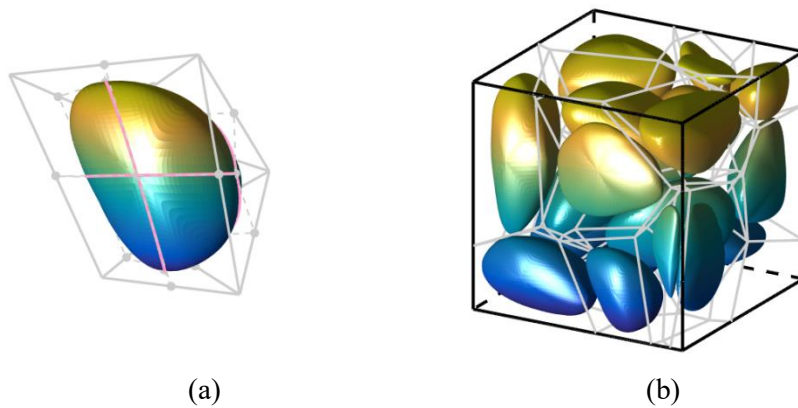(a)   (b)

Fig. 8   The generated solid particle with closed surface

2.4 Producing concavity with spherical harmonics

Based on the above procedure, irregular convex granular particles with smooth surfaces are generated.

Since the surface of a real particle frequently exhibits concavity features, the spherical harmonics are

employed here to introduce extra concavity features onto the smooth surface of each generated particle.

The spherical harmonic transform (SHT), which is essentially a (2D) Fourier transform onto 3D

sphere [44], has shown potential for characterizing the shapes of granular particles [45]. Previous

researchers [46-48] have indicated that an inverse operation of SHT can be performed to reconstruct a

virtual particle with specified shape features based on the presumed harmonic coefficient matrices. The

16

251   idea of the SHT is to expand the polar radius of the particle surface from a unit sphere and to calculate

252   the associated coefficients of the spherical harmonic series:

$$r(\theta, \varphi) = \sum_{n=0}^{N} \sum_{m=-n}^{n} c_n^m Y_n^m(\theta, \varphi) \tag{31}$$

253   where $r(\theta, \varphi)$ is the polar radius from the particle center with the corresponding spherical coordinates

254    $\theta \in [0, \pi]$ and $\varphi \in [0, 2\pi]$, which can be obtained by the coordinate transformation of the particle

255   surface vertices $V(x, y, z)$. c_n^m is the associated harmonic coefficient that requires determination, N

256   is the total number of harmonic frequencies, and $Y_n^m(\theta, \varphi)$ is the spherical harmonic function given

257   by:

$$Y_n^m(\theta, \varphi) = \sqrt{\frac{(2n+1)(n-m)!}{4\pi(n+m)!}} P_n^m(\cos \theta) e^{im\varphi} \tag{32}$$

258   where n and m are the frequency and the order of the associated Legendre function $P_n^m(x)$,

259   respectively, which can be expressed by Rodrigues's formula:

$$P_n^m(x) = (1 - x^2)^{|m|/2} \cdot \frac{d^{|m|}}{dx^{|m|}} \left[\frac{1}{2^n n!} \cdot \frac{d^n}{dx^n} (x^2 - 1)^n \right] \tag{33}$$

260   According to Eq. (31), the total number of c_n^m is $(N+1)^2$. Taking the discrete values of $r(\theta, \varphi)$

261   as the input on the left side of Eq. (31), a linear equation system with $(N+1)^2$ unknowns is obtained.

262   Then the optimized solution of c_n^m can be easily determined by adopting the standard least-squares

263   estimation for the linear equation system. Finally, the inverse operation of SHT can be conducted to

264   reconstruct the particle through the input of the obtained harmonic coefficients c_n^m on the right side of

265   Eq. (31) to compute the reconstructed continuous surface points $r'(\theta, \varphi)$.

266   Previous works have shown that particle morphological features can be constructed by

267   accumulating the decomposed spherical harmonic series with certain number of frequencies and

268   specified amplitudes. According to [48], the amplitude of the input harmonic coefficients c_n^m at each

269   frequency n determines different aspects of the reconstructed morphological features. The amplitude

270   A_n at each frequency n can be computed as:

$$A_n = \sqrt{\sum_{m=-n}^{n} \|c_n^m\|^2} \tag{34}$$

271   where $\|c_n^m\|$ is the second-order norm of c_n^m.

272   Specifically, as stated in [48], A_0 represents the particle size, A_1 does not influence the spherical

273   harmonic-reconstructed particle morphology, A_2 to A_4 represent the general shape of the particle at

274   a large-scale level, and A_5 to A_{15} represent the local concavity feature at a small-scale level.

275   Based on the inverse operation of SHT as introduced above, the spherical harmonic series (when

276        $5 \leq n \leq 15$) with coefficients c_n^m of amplitudes A_5 to A_{15} are employed to introduce concavity

277   features to the generated smooth particle surface. According to [48], a linear relationship between A_n

278   and n ($5 \leq n \leq 15$) in the log-log scale is assumed here:

$$A_n = K_A \cdot r_{ave} \cdot \left(\frac{n}{2}\right)^{2FD-6} \qquad \text{when } 5 \leq n \leq 15 \tag{35}$$

279   where K_A is the parameter that controls the amplitudes of the harmonic coefficients at frequencies from

280   5 to 15, r_{ave} is the average radius of the generated smooth surface particle, and FD is the fractal

281   dimension coefficient, which can be selected from the typical FD value ranges of Leighton Buzzard

282   sand ($2.043 \leq FD \leq 2.169$) and highly decomposed granite ($2.195 \leq FD \leq 2.377$), as recommend

283   by [48].

284   The procedure to produce concavity features on the generated convex particle is detailed as follows:

285   (1) Discretize the smooth surface of the generated convex shape particle into densely distributed

286   discrete points. Transform the coordinates of the points from the Cartesian coordinate system

287   into the spherical coordinate system;

288   (2) Calculate the mean radius of the surface points r_{ave};

289   (3) Determine the desired A_n ($5 \leq n \leq 15$) based on Eq. (22) and the selected K_A and FD;

290   (4) Generate a series of random numbers for the normalized harmonic coefficients at each degree

291   n, $c'_n = (c'^{-n}_n, c'^{-n+1}_n, \dots, c'^0_n, \dots, c'^{n-1}_n, c'^n_n)$ where c'^m_n ($-n \leq m \leq n$) are random

292   variables uniformly distributed from -1 to 1;

293   (5) Calculate the normalized amplitude of the random harmonic coefficients:

$$A'_n = \sqrt{\sum_{m=-n}^{n} (c'^m_n)^2} \tag{36}$$

294   (6) Determine the final harmonic coefficients c_n at each degree:

$$c_n = (c_n^{-n}, c_n^{-n+1}, \dots, c_n^0, \dots, c_n^{n-1}, c_n^n) \tag{37}$$

$$c_n^m = \frac{A_n}{A'_n} c'^m_n \tag{38}$$

295   (7) Calculate $Y_n^m(\theta, \varphi)$ for $\theta \in [0, \pi]$ and $\varphi \in [0, 2\pi]$ following Eq. (19), and calculate

296        $r'(\theta, \varphi)$ based on $r(\theta, \varphi)$, c_n^m, $Y_n^m(\theta, \varphi)$, r_{ave} and the following equation:

19

$$r'(\theta, \varphi) = r(\theta, \varphi) \cdot \left[1 + \left(\sum_{n=5}^{15} \sum_{m=-n}^{n} c_n^m Y_n^m(\theta, \varphi) \Big/ r_{ave} \right) \right] \tag{39}$$

297   Fig. 9 shows a unit sphere $r_{ave} = 1$ with imposed concavity features generated by the proposed

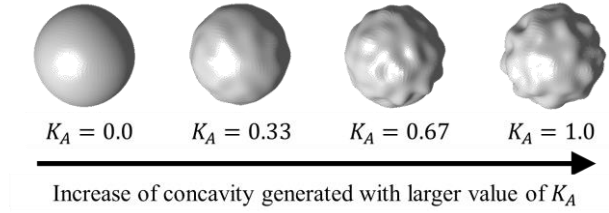298   spherical harmonic series at $n = 5$ to $n = 15$ for different K_A values.

$K_A = 0.0$ $K_A = 0.33$ $K_A = 0.67$ $K_A = 1.0$

Increase of concavity generated with larger value of K_A

299

300   Fig. 9   Producing concavity on a sphere based on the proposed inverse operation of SHT with

301   various K_A values

302   3 Control of the generated particle geometry

303   This section aims to illustrate how the volumetric size and different shape features of the generated

304   particles can be quantitatively and independently controlled based on the relationship between the

305   conventional geometry descriptors and the control parameters of the proposed algorithm.

306   3.1 Control of size and form parameters

307   First, we focus on the size and the form shape of the particle. The size of the particle, denoted as average

308   radius, r_{ave}, is computed from the radius of an equivalent sphere with the same volume:

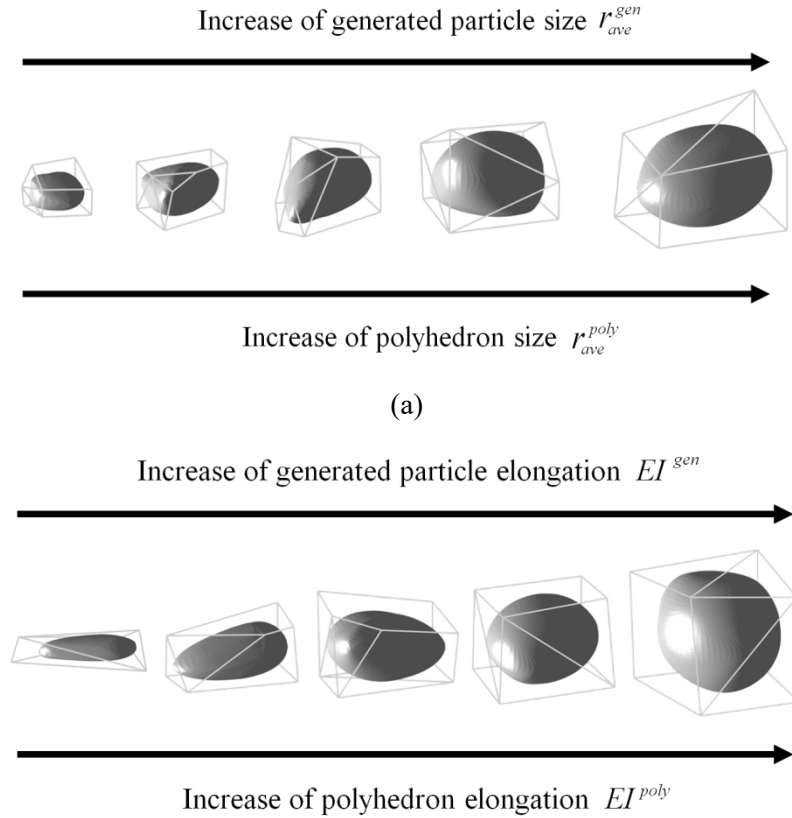$$r_{ave} = \left(\frac{3V}{4\pi} \right)^{\frac{1}{3}} \tag{40}$$

309   For the form shape, the elongation index, (EI), and flatness index, (FI), are employed to quantify

310   the dimensional ratio of the particle:

$$EI = \frac{I}{L} \tag{41}$$

$$FI = \frac{S}{I} \tag{42}$$

311   where S, I, and L are the minor, intermediate and major pricipal dimension of the particle,

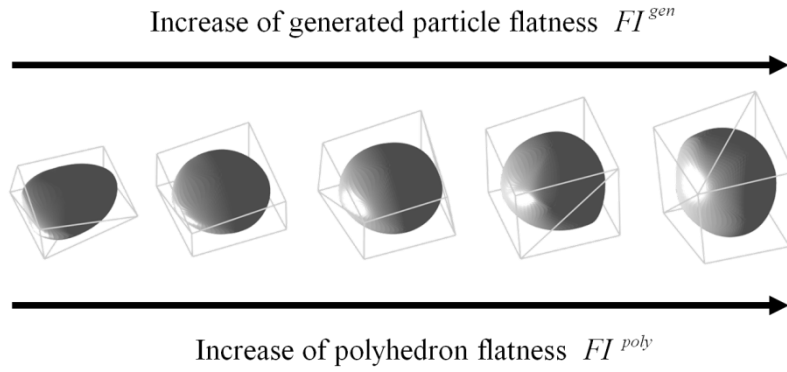312   respectively.

313   Since the generated particle approximates the given polyhedron to some extent, r_{ave}^{gen} EI^{gen} and

314   FI^{gen} are expected to be correlated with those of the circumscribed polyhedron, r_{ave}^{poly}, EI^{poly} and

315   FI^{poly}, respectively. Fig. 10a-c illustrates some example particles, which are generated inside

316   polyhedrons of various r_{ave}^{poly}, EI^{poly} and FI^{poly} values. It can be seen from the figure that the

317   polyhedrons with higher r_{ave}^{poly}, EI^{poly} and FI^{poly} values tend to produce particles with higher r_{ave}^{gen}

318   EI^{gen} and FI^{gen} values, respectively.

319

320   (a)

321

21

322

(b)

Increase of generated particle flatness FI^{gen}

323   Increase of polyhedron flatness FI^{poly}

324   (c)

325   Fig. 10   Illustration of example particles generated inside polyhedron of various (*a*) r_{ave}^{poly}, (*b*)

326   EI^{poly} and (*c*) FI^{poly}.

327   To further verify the capability to adjust the sizes and form shapes by controlling of the polyhedron

328   geometry, 1000 polyhedrons of various sizes ($r_{ave}^{poly} \in [1, 5]$), elongations $EI_{ave}^{poly} \in [0.2, 1]$ and

329   flatness values $FI_{ave}^{poly} \in [0.2, 1]$ are generated. For each polyhedron, a random variable w, that

330   follows a uniform distribution ranging from 0.1 to 1.0 is assigned to generate the smooth surface particle.

331   Then the r_{ave}^{gen}, EI^{gen}, FI^{gen} values for all the particles are computed. The influences of (*a*) r_{ave}^{poly},

332   (*b*) EI^{poly} and (*c*) FI^{poly} on the obtained r_{ave}^{gen}, EI^{gen}, and FI^{gen}, respectively, are shown in Fig.

333   11. As expected, r_{ave}^{poly}, EI^{poly} and FI^{poly} exhibit a strong linear relation with r_{ave}^{gen}, EI^{gen}, and

334   FI^{gen}, respectively. The equations of the generated size and shape values of particles as the functions

335   of the corresponding control parameters of polyhedrons are obtained from regression analysis and are

336   listed as follows:

$$r_{ave}^{gen} = 0.770 r_{ave}^{poly} - 0.037 \tag{43}$$

$$EI^{gen} = 0.872 EI^{poly} + 0.852 \tag{44}$$

$$FI^{gen} = 0.853 FI^{poly} + 0.989 \tag{45}$$

337   Based on the above equations, r_{ave}^{poly}, EI^{poly} and FI^{poly} can thus be used to control the

338   preliminary size and form shapes of the generated particle. More accurate control can be implemented

339   based on the inverse adjustment of individual polyhedron geometry as detailed in the author's previous

340   work [49] and concluded in section 4.1.

341
342   (a)

343
344   (b)

345
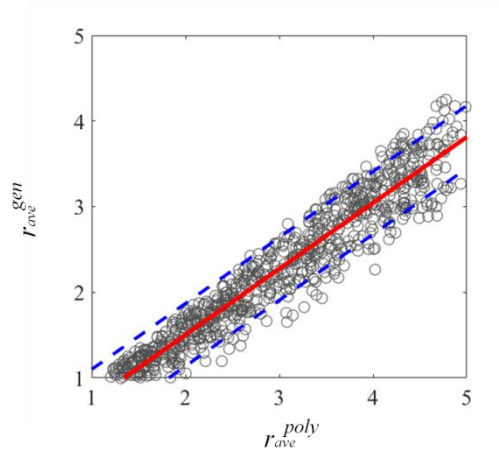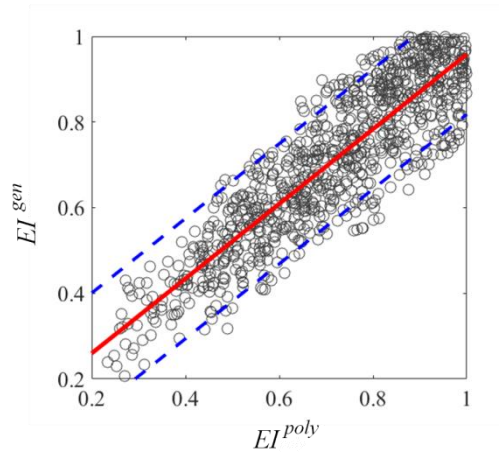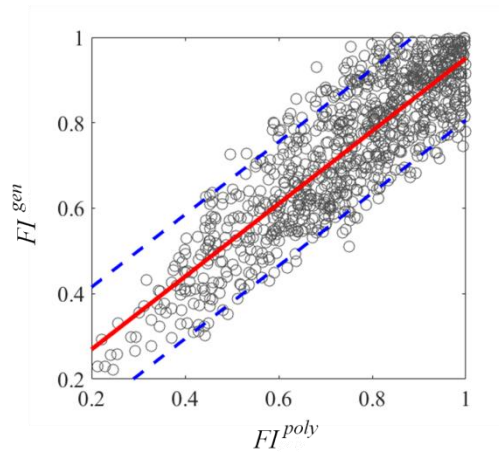
(c)

Fig. 11 Influences of control parameters (a) r_{ave}^{poly}, (b) EI^{poly} and (c) FI^{poly} on the (a) r_{ave}^{gen}, (b) EI^{gen} and (c) FI^{gen} of the generated particles. Solid line: mean values; dotted lines: mean values +/- one standard deviation

3.2 Control of the corner sharpness parameter

The sharpness of the corners is known to influence the kinematics, e.g., sliding and rolling [50], of the particles. In this section, we illustrate the capability of the proposed algorithm to control the corner sharpness of the generated particle. The 3D Wadell's roundness is computed to quantify the corner sharpness [51]:

$$R = \frac{\sum r_i}{n R_{insc}} \tag{46}$$

where R_{insc} is the radius of the maximum inscribed circle, r_i is the radius of the ith sphere which is fitted to the corner of the particle, and n is the total number of spheres that fit all the identified particle corners. Fig. 12 illustrates four example particles with various corner sharpness values generated by different value of w, where w ranges from 0.1 to 0.4, and R increases from 0.16 to 0.65.

Particles generated by assining larger value of Bezier curve parameter

w = 0.4   w = 0.3   w = 0.2   w = 0.1

R = 0.65   R = 0.54   R = 0.39   R = 0.16

Increase of corner sharpness, e.g., smaller value of Wadell's roundness
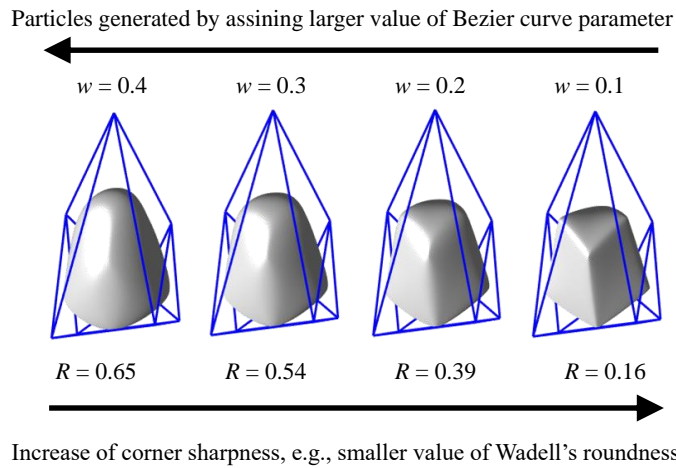
Fig. 12 Example particle of various corner sharpness generated by different value of w

To further verify the capability of adjusting the corner sharpness with the control parameter w, 1000 polyhedrons of various elongation and flatness are generated. For each polyhedron, a random

363   variable w, that follows a uniform distribution ranging from 0.1 to 1.0 is assigned to generate the

364   smooth surface particle of different corner sharpness features. Then the R values for all the particles

365   are computed. The influences of w on the obtained R values, as well as those on EI^{gen} and FI^{gen},

366   is shown in Fig. 13. As expected, R exhibits a strong inverse-U-shape relation with w. Based on the

367   obtained data, the polynomial regression equation for relating w to R is derived as follow:

$$R = -1.563w^3 + 0.038w^2 + 1.698w - 0.063 \tag{47}$$

368   Thus, with the above equation and inverse parameter adjustment, w can be used to control the

369   corner sharpness R of the generated particle.
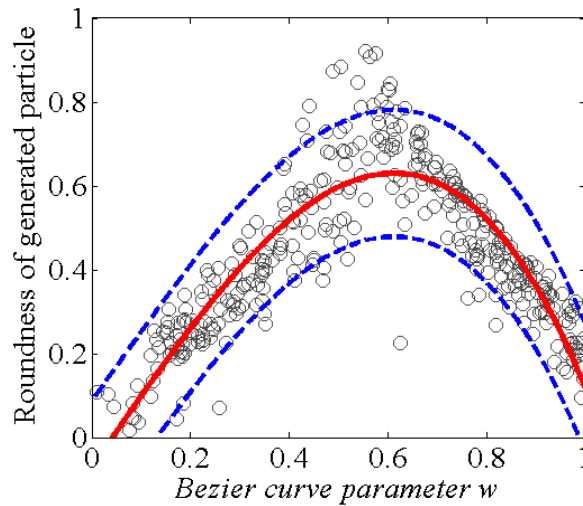

370
371   Fig. 13   Influence of control parameter w on roundness of generated particles. Solid line: mean
372   values; dotted lines: mean values +/- one standard deviation

373   3.3 Control of concavity parameter

374   The convexity ratio (CR) characterizes the concavity feature, which is known to influence the amount

375   of interlocking at contacts between two neighboring particles. For a 3D particle, it is calculated as:

$$CR = \frac{V_{particle}}{V_{convex}} \tag{48}$$

376   where $V_{particle}$ is the volume of the particle, and V_{convex} is the volume of the convex hull of the

377   particle. In this section, we illustrate the capability of the proposed algorithm to reproduce particles

378   with desired concavity features using the spherical harmonics of different control parameters K_A. First,

379   the example particles generated by different control parameters w and K_A are shown in .Fig. 14.
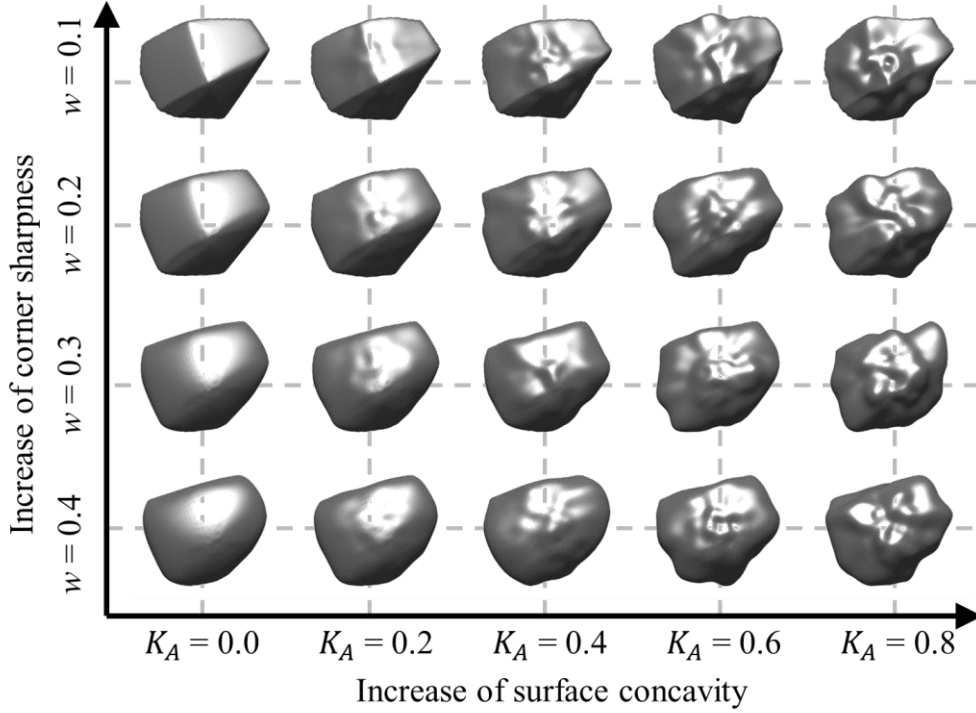

380

381   Fig. 14   Illustration of particles generated by different control parameters w and K_A

382   To further verify the capability of adjusting the particle concavity, the correlations between the

383   convexity ratio of the generated particles and the control parameter K_A are examined. In this section,

384   the previously generated 1000 smooth surface particles ($CR = 0$) with various elongation, flatness and

385   roundness values are used as the parent particles. For each parent, 10 particles are generated with

386   various values of K_A, which follows a uniform distribution ranging from 0 to 1.0. The influences of K_A

387   on the obtained CR^{gen} are shown in Fig. 15. As expected, the K_A exhibits a strong negative relation

388   with CR^{gen}. The regression equation for controlling of CR^{gen} with K_A can be obtained:

26

$$CR^{gen} = -0.026 K_A{}^3 - 0.493 K_A{}^2 - 0.146 K_A - 0.999 \tag{49}$$

389 Subsequently, using this equation, when the desired convexity ratio CR^{tar} is given, the

390 corresponding K_A can be easily determined. If there is any discrepancy between the generated

391 convexity ratio CR^{gen} and the target value, the inverse adjustment can always be performed to
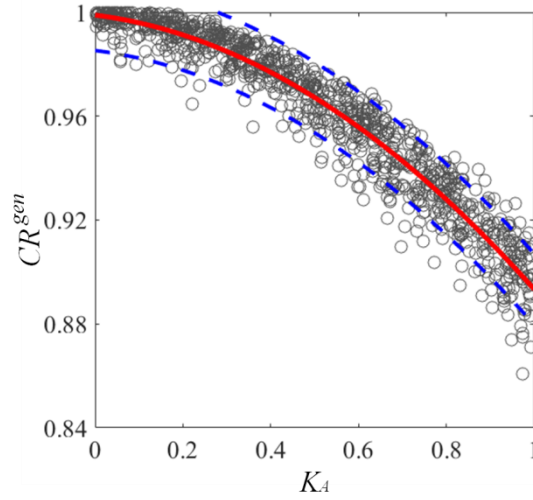
392 accurately control the error.

393

394 Fig. 15 Influence of control parameter K_A on concavity (CR) of generated particles. Solid line:
395 mean values; dotted lines: mean values +/- one standard deviation

396 4 Random packing of the generated irregular particles

397 4.1 Proposed scheme for generation of particle packing

398 In this study, the proposed algorithm to generate the random packing of nonspherical particles with

399 desired geometric features includes the following major steps:

400 (1) First, irregular-shape polyhedrons with desired size, elongation and flatness values are generated

401 through the constrained Voronoi tessellation method [49]. The method is alternative to the normal

402 Voronoi tessellation method and is based on the controlled partition of the virtual container by the means

403   of a constrained Voronoi tessellation. The method was inspired by the IMC framework initially appeared

404   in [52]. The constrained Voronoi tessellation comprises the following sub-steps:

405   (i)   Generate an initial set of points within the selected domain, and perform a bounded

406   Voronoi tessellation (i.e. the union of all the cells is identical to the whole domain).

407   (ii)   Evaluate the geometric properties of the obtained Voronoi polyhedron, e.g., r_{ave}^{poly}, EI^{poly}

408   and FI^{poly}. Compute the error corresponding to the differences between the current values

409   and the targets, (r_{ave}^{tar}, EI^{tar} and FI^{tar}).

410   (iii) Randomly move one of the seeding points to another random location, compute the new

411   tessellation with only modifying the local cells around the moving point [49], and repeat

412   step (ii). If the error is less than its previous value, accept the modification; otherwise reject

413   it.

414   (iv)   Repeat step (iii) until the error has reached an acceptable value. Indeed, there would still

415   be a certain discrepancy between the generated particles and the targets. Thus, the above

416   procedure can be performed again to minimize the error between those the generated

417   particles (r_{ave}^{gen}, EI^{gen} and FI^{gen}), and the desired targets, (r_{ave}^{tar}, EI^{tar} and FI^{tar}).

418   (2) Next, the key points are extracted from the edges and facets of the polyhedrons. According to the

419   target corner sharpness (R^{tar}), the Bézier curves are generated with certain control parameter w to

420   form curve networks inside the polyhedrons. Then, an irregular nonspherical particle surface is

421   generated based on Gregory surface interpolation.

422   (3) Based on the target convexity (CR^{tar}), superimpose the spherical harmonics with appropriate K_A

423   values on the particle surface to produce convexity features.

424   (4) Finally, compute the error corresponding to the differences between the current and target ones.

425   Adjust the shape control parameters w, and K_A, until the error reaches an acceptable value.

426

427   4.2 Examples of generated particle packing

428   To comprehensively demonstrate the capability of the proposed algorithms for studying granular

429   materials, three scenarios of particle packing are provided in this subsection: (1) packing of bidispersed

430   particle mixtures with various coarse-particle weights and different size ratios, (2) packing of realistic

431   particles with distinctive shape features, and (3) packing of quantitatively controlled particle

432   orientations and form scale shapes.

433   (1) Packing of bidispersed particle mixtures

434   Bidispersed particle mixtures with various combinations of coarse and fine grains are simulated

435   using the proposed method. The simulated particles can be considered as binary mixtures of sands and

436   gravels with sufficiently large interparticle stiffness and cohesionless interparticle contacts. The binary

437   mixture can be characterized by two important parameters, the weight of the coarse grains, W_C, and

438   the grain size ratio, α_V:

$$W_C = \frac{V_{coarse}}{V_{total}} \tag{50}$$

439   where V_{coarse} represents the sum of the volume of the coarse particles, and V_{total} represents the total

440   volume of the coarse and fine particles, and

$$\alpha_V = \frac{\mu(D_{coarse})}{\mu(D_{fine})} \tag{51}$$

29

441   where $\mu(D_{coarse})$ denotes the mean diameter of the coarse grains, and $\mu(D_{fine})$ denotes the mean
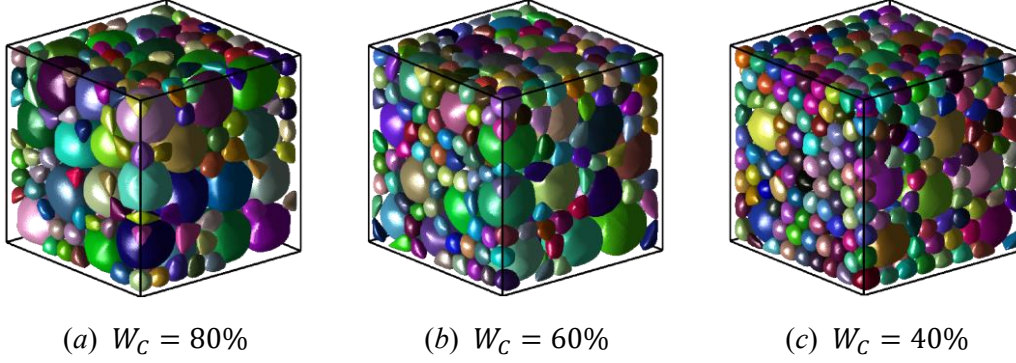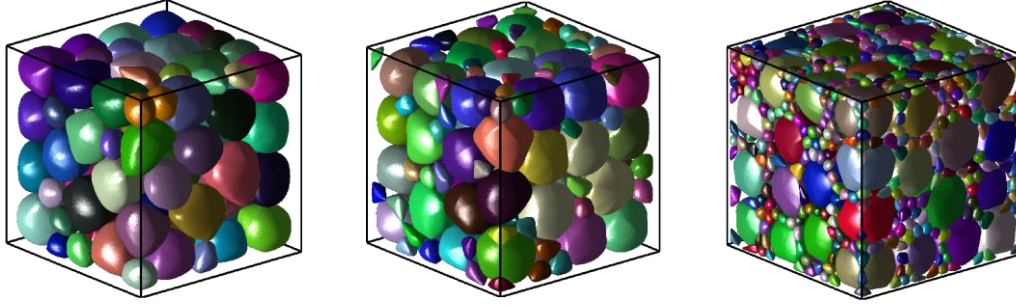
442   diameter of the fine grains.

443

444   (*a*) $W_C = 80\%$ (*b*) $W_C = 60\%$ (*c*) $W_C = 40\%$
445   Fig. 16   Packing patterns of the generated binary mixture with different volumetric size ratio (*a*)
446                        $W_C = 80\%$, (*b*) $W_C = 60\%$ and (*c*) $W_C = 40\%$

447   In total 6 samples are produced to illustrate the capability of the proposed method to simulate

448   bidispersed particles with different values of W_C and α_V. The bidispersed binary particle mixtures

449   have different coarse grain weights ($W_C = 80\%$, 60%, 40%) and grain size ratios ($\alpha_V = 1\!:\!1$, $2\!:\!1$,

450    $3\!:\!1$); the packing patterns are illustrated in Fig. 16 and Fig. 17, respectively. The figures show that the

451   proposed method can efficiently and effectively produce bidispersed particle mixtures with various

452   coarse grain weights and grain size ratios. Since many geotechnical researchers are very interested in

453   binary mixture (gap graded soils), and the generation of initial packing for such material was the main

454   problem that influence the computational time in their simulations, we demonstrate the bi-disperse

455   packings for illustration purpose. It should be noted that the algorithm can actually generate a wide

456   range of particle size distribution. The capability and validity of the IMC algorithm to control the

457   Voronoi cell size distributions are detailed in [49].

458

459   (*a*) $\alpha_V = 5:3$ (*b*) $\alpha_V = 5:2$ (*c*) $\alpha_V = 5:1$

460   Fig. 17   Packing patterns of the generated binary mixture with different volumetric size ratio (*a*)

461                      $\alpha_V = 5:3$, (*b*) $\alpha_V = 5:2$ and (*c*) $\alpha_V = 5:1$

462   (2) Packing of particles that have realistic shapes
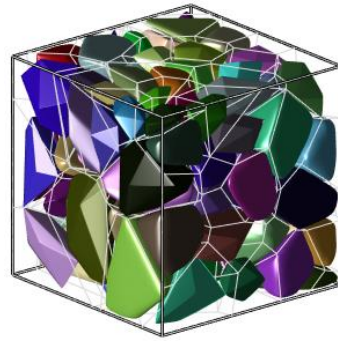
463   Four examples of particle packing, composed of 100 particles each, are generated with the

464   following realistic and distinctive features: (1) the first example aims to generate particles with high

465   corner sharpness and large concavity values, (2) the second example focuses on producing particles

466   with sharp corners without concavity, (3) the third example generates particles with low corner

467   sharpness with larger concavity, and (4) the fourth example produces particles with rounded corners

468   and smooth surfaces. The properties related to the corner sharpness and concavity are acquired by

469   carefully adjusting the control parameters w and K_A. The clearly recognizable differences between

470   the four examples are visualized in Fig. 18*a-h*. The grain shapes of the first example are somehow

471   similar to those of crushed rocks in Fig. 18*b*, while those of the second example are more often

472   encountered in grinding materials, e.g., the brown fused alumina in Fig. 18*d*. The shapes of the third

473   example approximate those of the quartz sands, in Fig. 18*f*., whilst the particles in the fourth example

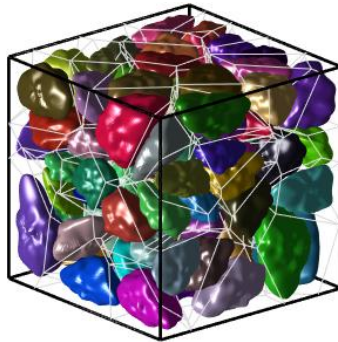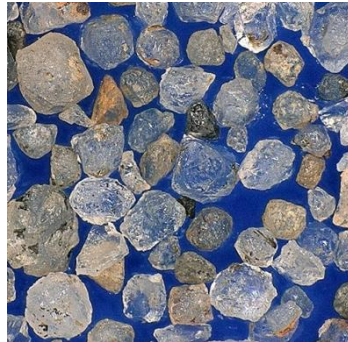474   are more identical to riverbank pebbles, in Fig. 18*h*.

475

476   (a)   (b)

477

478   (c)   (d)

479

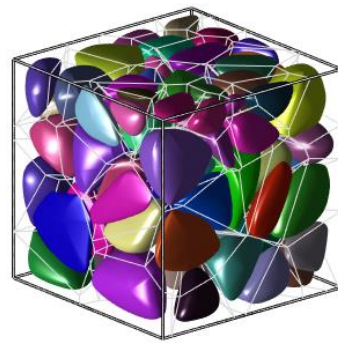480   (e)   (f)

481

482   (g)   (h)
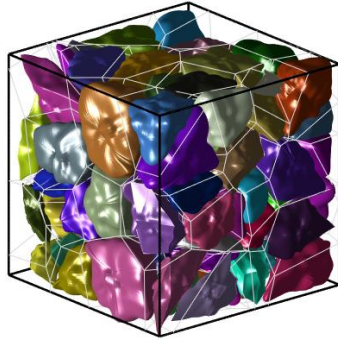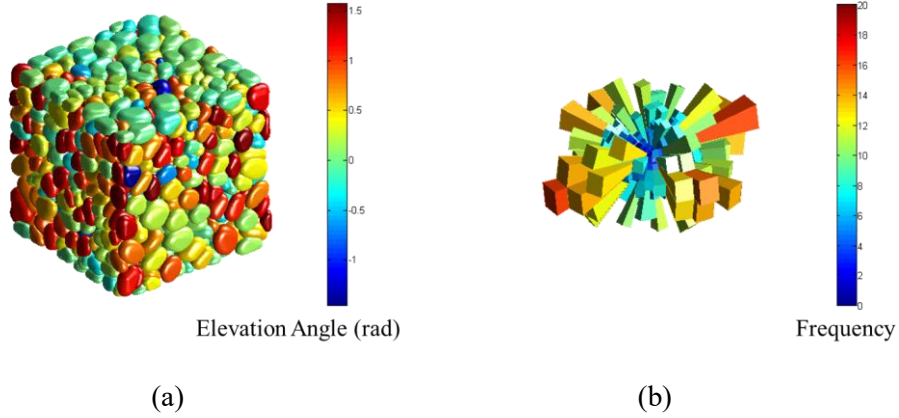
483   Fig. 18   Four examples of packing with distinctive particle shapes
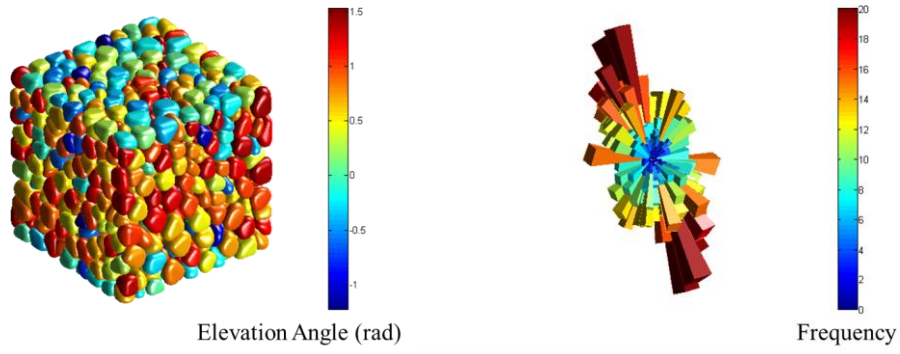
484   (3) Packing of particles having prescribed geometrical values

485   Two groups of particle packing are presented at this scenario to illustrate the potential of proposed

486   algorithm. They make use of the illustrative geometry controlling scheme as presented in the previous

487   sections. Each group has the following prescribed distinctive features:

488   Group 1: Particles with desired orientations, e.g., isotropic orientated ($\theta \in [-\pi, \pi]$, $\varphi \in \left[-\frac{\pi}{2}, \frac{\pi}{2}\right]$),

489   vertical orientated ($\theta \in [-\pi, \pi]$, $\varphi \to -\frac{\pi}{2}$ or $\frac{\pi}{2}$), and horizontal orientated ($\theta \in [-\pi, \pi]$, $\varphi \to 0$).

490   As illustrated in Fig. 19*a-b*, at initial stage, the reconstructed particles based on the Voronoi cells

491   tend to have random orientations. Then, after a few numbers of iterations, as shown in Fig. 19*c-d*, the

492   generated particles gradually become vertically orientated. The final results are demonstrated in Fig.

493   19*e-f*, where the particles assembly displays identical orientations to the desired values, $\theta \in [-\pi, \pi]$,

494    $\varphi \to -\frac{\pi}{2}$ or $\frac{\pi}{2}$.

495

Elevation Angle (rad)   Frequency

496
497   (a)   (b)

33

Elevation Angle (rad)

Frequency

498
499   (c)   (d)

Elevation Angle (rad)

Frequency
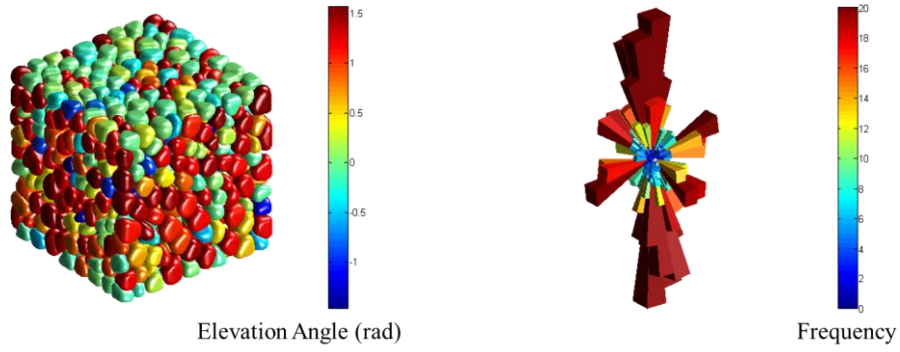
500
501   (e)   (f)
502   Fig. 19   Generation of vertical orientated particles: (*a*) ~ (*b*) Initial stage; (*c*) ~ (*d*) Intermediate
503   stage; (*e*) ~ (*f*) Final stage

504   The evolutions of the generated particles and their orientation diagrams for horizontal orientated

505   and isotropic orientated spatial distributions are illustrated in Fig. 20 and Fig. 21, respectively. The

506   results prove that the proposed algorithm has good performance in generating particles packing with

507   predetermined spatial orientations.

Elevation Angle (rad)

Frequency

508
509   (a)   (b)

34

510

511   (c)   (d)

512
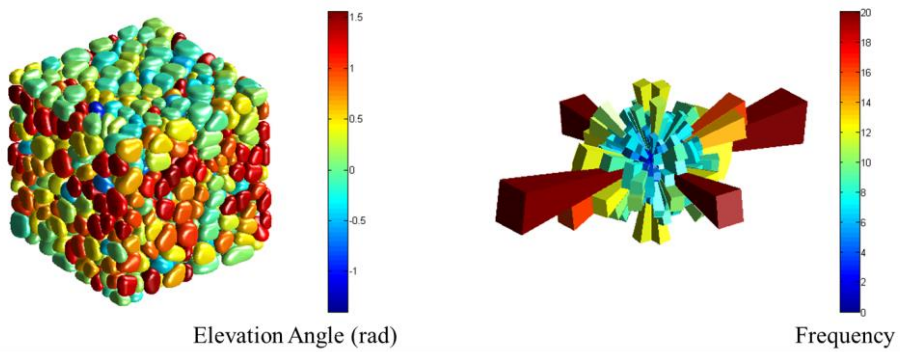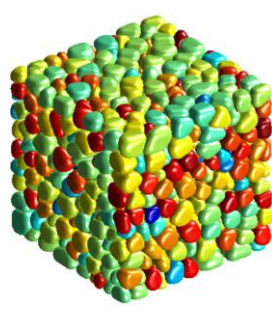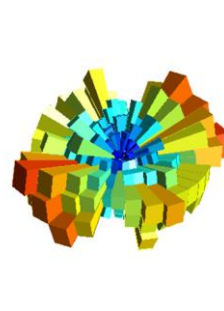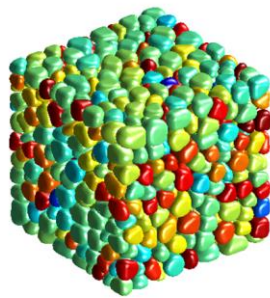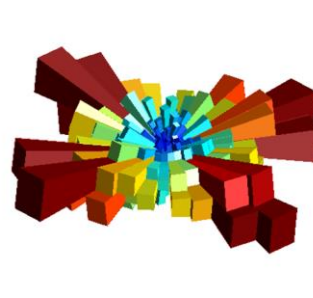
513   (e)   (f)

Fig. 20   Generation of horizontal orientated particles: (*a*) ~ (*b*) Initial stage; (*c*) ~ (*d*) Intermediate

stage; (*e*) ~ (*f*) Final stage

516

517

518   (a)   (b)   (c)

519

520   (d)   (e)   (f)

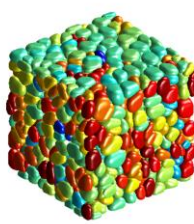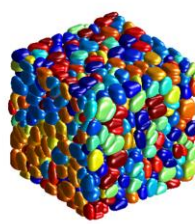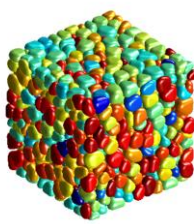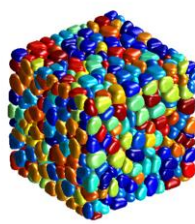Elevation Angle (rad)   Azimuth Angle (rad)   Frequency

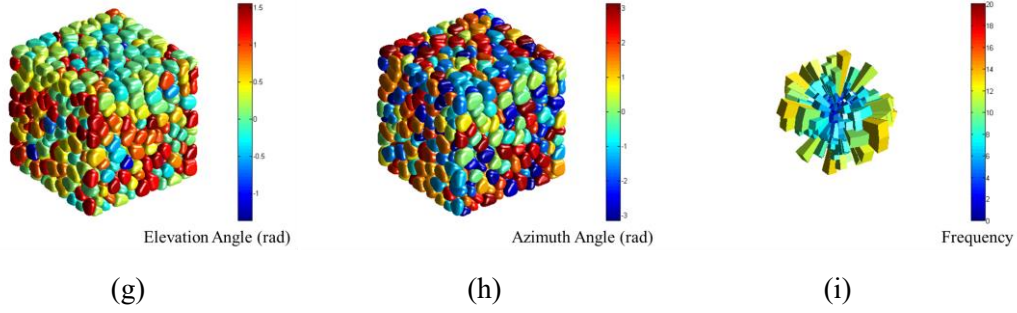(g)   (h)   (i)

Fig. 21   Generation of isotropic orientated particles: (a) ~ (c) Initial stage; (d) ~ (f) Intermediate stage; (g) ~ (i) Final stage

Group 2: Particles with desired elongations and flatness, e.g., oblate ($\mu_{EI} = 0.9$, $\sigma_{EI} = 0.06$; $\mu_{FI} = 0.5$, $\sigma_{FI} = 0.06$), prolate ($\mu_{EI} = 0.5$, $\sigma_{EI} = 0.06$; $\mu_{FI} = 0.9$, $\sigma_{FI} = 0.06$) and scalene ($\mu_{EI} = 0.5$, $\sigma_{EI} = 0.06$; $\mu_{FI} = 0.5$, $\sigma_{FI} = 0.06$). The error function between the generated EI, FI distributions and their corresponding targets are defined as:

$$\text{Error} = \int_0^1 \left| pdf_{tar}(x) - pdf_{gen}(x) \right| dx \tag{52}$$

where $pdf_{tar}(x)$ is the target probability density function of the chosen shape index, $pdf_{gen}(x)$ is the generated probability density function of the chosen shape index. Following the author's previous work in [36], the integral is computed numerically using discretized versions of the probability density function, and a target value of 0.1 can provide satisfactory results.

As displayed in Fig. 22a-b, at the initial stage, the particles reconstructed from the original Voronoi cells exhibit quite random distributions of elongation and flatness, $EI \in [0.4, 1.0]$, $FI \in [0.1, 1.0]$. The errors between the generated EI, FI values and their corresponding targets were 0.78 and 1.82, respectively. Then, after the geometry adjustment algorithm is applied, as illustrated in Fig. 22c-d, the mean value of elongation increases from 0.81 to 0.85, while the mean of flatness significantly decreases from 0.79 to 0.55. The errors for both EI and FI also decrease to about 0.5. Finally, as illustrated in

36

539   Fig. 22*e-f*, the generated specimen exhibits *EI* and *FI* values approach very close to the desired

540   distributions, with satisfied errors around 0.1.

541
542   (a)   (b)

543
544   (c)   (d)

545
546   (e)   (f)

547   Fig. 22   Generation of oblate shape particles: : (*a*) ~ (*b*) Initial stage; (*c*) ~ (*d*) Intermediate stage; (*e*)
548   ~ (*f*) Final stage

549   As for the prolate and scalene cases, the changes of the shape distributions from initial stage to

550   final stage, which are processed by the proposed algorithm, are also illustrated in Fig. 23 and Fig. 24,

551   respectively. The generated prolate particles present errors of *EI* and *FI* decreasing from 1.83 to 0.11

552   and 0.54 to 0.14, while the generated scalene particles exhibit errors of *EI* and *FI* reducing from 1.84

553   to 0.11 and 1.83 to 0.09. They both display statistics of generated particle shapes gradually become

554   identical to the predetermined distributions. The above examples prove that the proposed algorithm has

555   very strong capability in generating particles packing that satisfies the prescribed targets of particle

556   shapes.

(a)   (b)

(c)   (d)

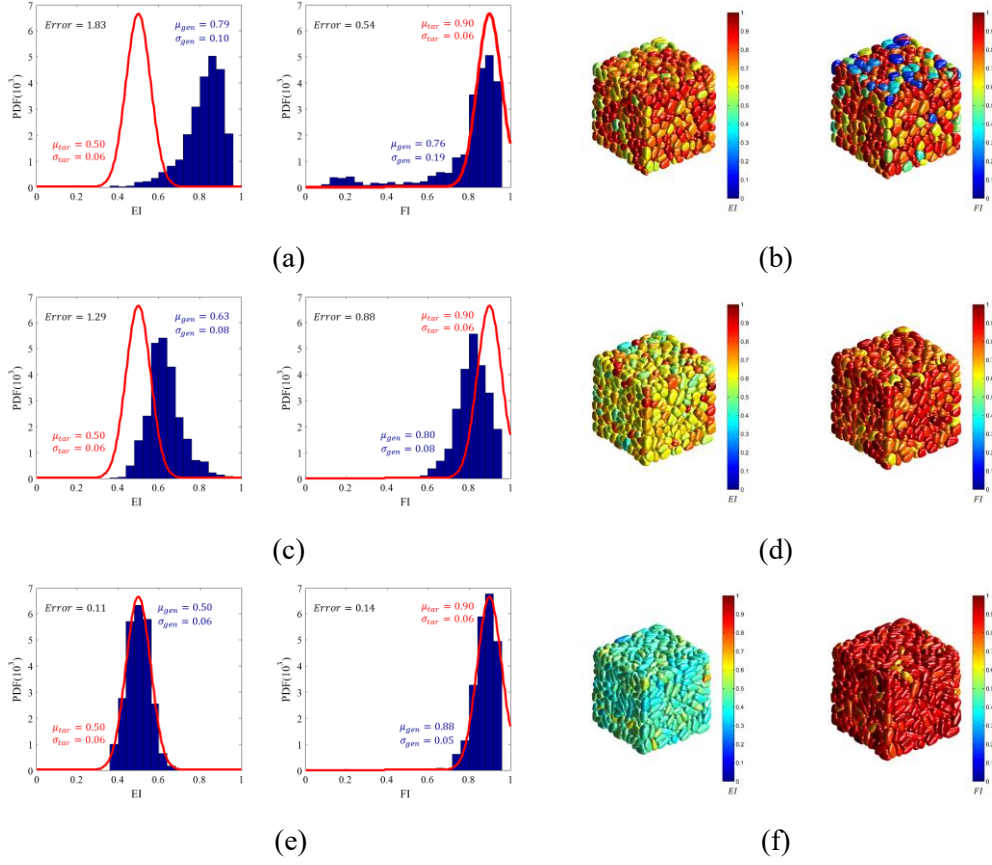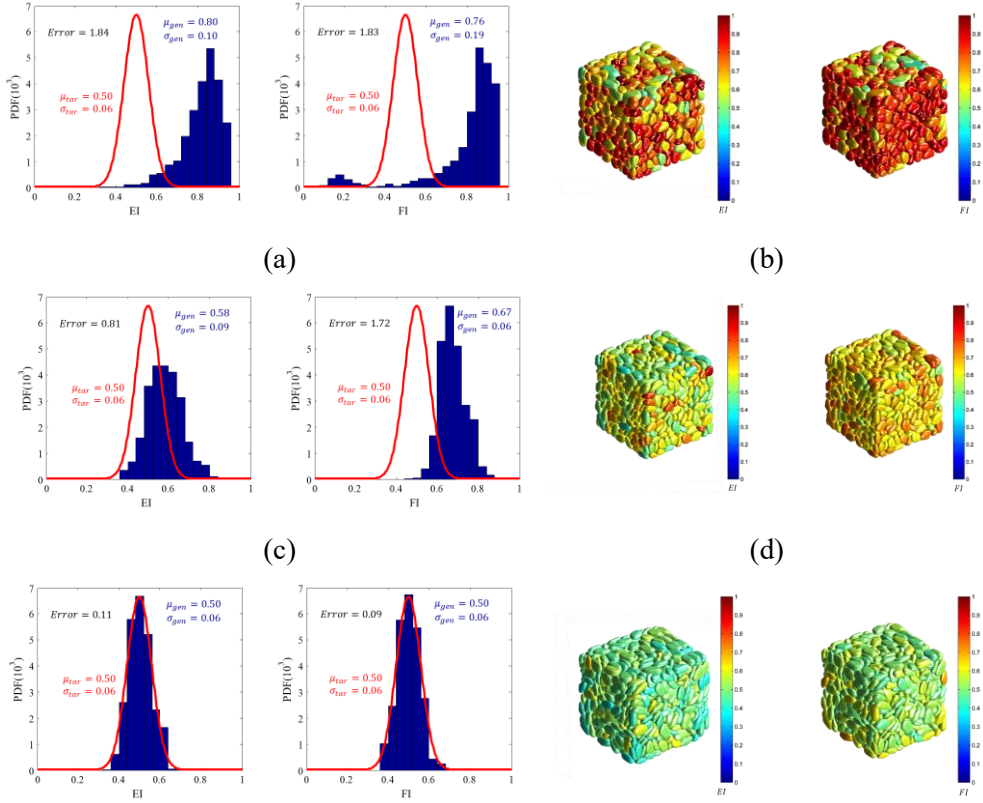(e)   (f)

Fig. 23   Generation of prolate shape particles: (*a*) ~ (*b*) Initial stage; (*c*) ~ (*d*) Intermediate stage; (*e*)
~ (*f*) Final stage

(a)   (b)

(c)   (d)

Fig. 24   Generation of scalene shape particles: (*a*) ~ (*b*) Initial stage; (*c*) ~ (*d*) Intermediate stage; (*e*) ~ (*f*) Final stage

5 Conclusion and discussion

In this paper, we proposed and combined a series of computational geometry algorithms (Voronoi tessellation, Bezier curve fitting and biharmonic-based surface interpolation) and spherical harmonic transformation for generation of non-spherical particles with controllable shape features for future numerical investigation of shape effects on granular behaviors. The quantitative control of size, elongation, flatness, corner sharpness and concavity is facilitated through the geometry modification of Voronoi polyhedron and adjustment of the control parameters w and K_A for particle generation. Three cases of particles packing are given to demonstrate the capabilities of the proposed approach. The first case illustrates the ability of proposed approach in producing bidispersed particle mixtures with various coarse grain weights and grain size ratios. The second case shows the capability of generating packing of realistic particles with distinctive shape features. The third case validates the geometry controlling capability of the prosed algorithms. All results prove that the proposed method is robust and efficient in generating realistic granular packing with desired grain sizes and distinctive particle shapes. It provides a basis for numerical simulation of different shape effects of natural granular materials on their mechanical, thermal and hydraulic properties.

In conclusion, the sample generation is a very important step of discrete element modeling, in particular for irregular particles and initial anisotropy of the sample. This study only focuses on the sample generation relating to the geometrical aspect of granular packing, and the part of granular mechanics will be followed in a future study. Indeed, there is a major challenge in implementation of further

592 numerical tests on the generated packing of particles in DEM. How to simulate irregular particles with

593 concave and convex shapes effectively and efficiently is still an open problem. Potential solutions

594 include overlapping-spheres-based DEM [53], NURBS-based DEM [54], level-set-based DEM [55],

595 etc. However, the computational loads of these discrete modeling techniques increase markedly with

596 the increasing complexity of the particle outline. Additionally, there will be a tradeoff between the

597 number of spheres/nodes and the fidelity of the simplified particle profile compared with the original

598 one. The simplifications should not alter the shape properties of interests. Based on the present work,

599 our future research will focus on: (1) incorporation of the proposed particle model into DEM code, e.g.,

600 developing an advancing contact detection approach that is suitable for arbitrary shape particles; (2)

601 investigating the individual effects of shapes, e.g., corner sharpness and concavity on the macro- and

602 micromechanical properties of granular materials based on the proposed particle models.

607 References

608 [1] F.N. Altuhafi, M.R. Coop, Changes to particle characteristics associated with the compression of
609   sands, Geotechnique, 61 (2011) 459-471.

610 [2] L. Wang, R. Li, B. Wu, Z. Wu, Z. Ding, Determination of the coefficient of rolling friction of an
611   irregularly shaped maize particle group using physical experiment and simulations, Particuology,
612   (2017).

613 [3] A. Tsomokos, V.N. Georgiannou, Effect of grain shape and angularity on the undrained response of
614   fine sands, Canadian Geotechnical Journal, 47 (2010) 539-551.

615 [4] X.W. Fu, D. Huck, L. Makein, B. Armstrong, U. Willen, T. Freeman, Effect of particle shape and

616   size on flow properties of lactose powders, Particuology, 10 (2012) 203-208.

617   [5] F.N. Altuhafi, M.R. Coop, V.N. Georgiannou, Effect of Particle Shape on the Mechanical Behavior
618   of Natural Sands, J. Geotech. Geoenviron. Eng., 142 (2016) 15.

619   [6] J.C. Santamarina, Soil behaviour: The role of particle shape, Thomas Telford, (2004).

620   [7] Vepraskas, M. J., D.K. Cassel, Sphericity and roundness of sand in coastal plain soils and
621   relationships with soil physical properties., Soil Science Society of America Journal, 51 (1987).

622   [8] C.J. Coetzee, Calibration of the discrete element method and the effect of particle shape, Powder
623   Technol., 297 (2016) 50-70.

624   [9] L. Tong, Y.H. Wang, DEM simulations of shear modulus and damping ratio of sand with emphasis
625   on the effects of particle number, particle shape, and aging, Acta Geotechnica, 10 (2015) 117-130.

626   [10] E. Tutumluer, H. Huang, Y.M.A. Hashash, J. Ghaboussi, Imaging based discrete element modeling
627   of granular assemblies, in: D.C. Univ Illinois, U.I.L.U.S.A. Environm Engn (Eds.) 9th International
628   Conference on Multiscale and Functionally Graded Materials, Amer Inst Physics, Oahu, HI, 2006,
629   pp. 544-549.

630   [11] Y. Yang, J.F. Wang, Y.M. Cheng, Quantified evaluation of particle shape effects from micro-to-
631   macro scales for non-convex grains, Particuology, 25 (2016) 23-35.

632   [12] W. Chaikittisilp, T. Taenumtrakul, P. Boonsuwan, W. Tanthapanichakoon, T. Charinpanitkul,
633   Analysis of solid particle mixing in inclined fluidized beds using DEM simulation, Chemical
634   Engineering Journal, 122 (2006) 21-29.

635   [13] K. Dong, C. Wang, A. Yu, A novel method based on orientation discretization for discrete element
636   modeling of non-spherical particles, Chemical Engineering Science, 126 (2015) 500-516.

637   [14] H.P. Zhu, Z.Y. Zhou, R.Y. Yang, A.B. Yu, Discrete particle simulation of particulate systems: A
638   review of major applications and findings, Chemical Engineering Science, 62 (2007) 3378-3396.

639   [15] J. Li, C. Webb, S.S. Pandiella, G.M. Campbell, Discrete particle motion on sieves—a numerical
640   study using the DEM simulation, Powder Technology, 133 (2003) 190-202.

641   [16] Y. Tsuji, T. Kawaguchi, T. Tanaka, Discrete particle simulation of two-dimensional fluidized bed,
642   Powder Technology, 77 (1993) 79-87.

643   [17] Y. He, T.J. Evans, A.B. Yu, R.Y. Yang, A GPU-based DEM for modelling large scale powder
644   compaction with wide size distributions, Powder Technology, 333 (2018).

645   [18] P.A. Cundall, O.D.L. Strack, A discrete numerical model for granular assemblies, Geotechnique,
646   29 (2008) 331-336.

647   [19] T.G. Sitharam, M.S. Nimbkar, Micromechanical Modelling of Granular Materials: Effect of
648   Particle Size and Gradation, Geotechnical & Geological Engineering, 18 (2000) 91-117.

649   [20] J. Gong, J. Liu, Mechanical transitional behavior of binary mixtures via DEM: Effect of differences
650   in contact-type friction coefficients, Computers & Geotechnics, 85 (2017) 1-14.

651   [21] M. Oda, J. Konishi, S. Nemat-Nasser, Experimental micromechanical evaluation of strength of
652   granular materials: Effects of particle rolling, Mechanics of Materials, 1 (1982) 269-283.

[22] L. Rothenburg, Micromechanical features of granular assemblies with planar elliptical particles, Geotechnique, 42 (1992) 79-95.

[23] T. Ueda, T. Matsushima, Y. Yamada, Effect of particle size ratio and volume fraction on shear strength of binary granular mixture, Granular Matter, 13 (2011) 731-742.

[24] T.-T. Ng, Numerical simulations of granular soil using elliptical particles, Computers and geotechnics, 16 (1994) 153-169.

[25] X. Lin, T.T. Ng, Contact detection algorithms for three-dimensional ellipsoids in discrete element modelling, International Journal for Numerical and Analytical Methods in Geomechanics, 19 (1995) 653-659.

[26] X. Lin, T.T. Ng, A three-dimensional discrete element model using arrays of ellipsoids, Géotechnique, 47 (1997) 319-329.

[27] J.Q. Gan, A.B. Yu, Z.Y. Zhou, DEM simulation on the packing of fine ellipsoids, Chemical Engineering Science, 156 (2016) 64-76.

[28] E. Azéma, F. Radjaï, Stress-strain behavior and geometrical properties of packings of elongated particles, Physical Review E Statistical Nonlinear & Soft Matter Physics, 81 (2010) 051304.

[29] A.V. Kyrylyuk, A.P. Philipse, Effect of particle shape on the random packing density of amorphous solids, Physica Status Solidi, 208 (2011) 2299-2302.

[30] L. Peng, S.X. Li, Z. Jian, L.Y. Meng, A computational investigation on random packings of sphere-spherocylinder mixtures, Science China Physics Mechanics & Astronomy, 53 (2010) 2284-2292.

[31] S. Zhao, N. Zhang, X. Zhou, L. Zhang, Particle shape effects on fabric of granular random packing, Powder Technology, 310 (2017) 175-186.

[32] K. Han, Y.T. Feng, D.R.J. Owen, Polygon-based contact resolution for superquadrics, International Journal for Numerical Methods in Engineering, 66 (2010) 485-501.

[33] W. Zhou, Y. Huang, T.T. Ng, G. Ma, A geometric potential-based contact detection algorithm for egg-shaped particles in discrete element modeling, Powder Technol., 327 (2017).

[34] J.F. Peters, M.A. Hopkins, R. Kala, R.E. Wahl, A poly-ellipsoid particle for non-spherical discrete element method, Eng. Comput., 26 (2009) 645-657.

[35] B. Nassauer, T. Liedke, M. Kuna, Polyhedral particles for the discrete element method, Granular Matter, 15 (2013) 85-93.

[36] G. Mollon, J. Zhao, 3D generation of realistic granular samples based on random fields theory and Fourier shape descriptors, Computer Methods in Applied Mechanics & Engineering, 279 (2014) 46-65.

[37] D. Su, W.M. Yan, 3D characterization of general-shape sand particles using microfocus X-ray computed tomography and spherical harmonic functions, and particle regeneration using multivariate random vector, (2017).

[38] B. Zhou, J. Wang, B. Zhao, Micromorphology characterization and reconstruction of sand particles using micro X-ray tomography and spherical harmonics, Engineering Geology, 184 (2015) 126-

690   137.

691 [39] X. Wang, J. Gong, A. An, K. Zhang, Z. Nie, Random generation of convex granule packing based
692   on weighted Voronoi tessellation and cubic-polynomial-curve fitting, Computers and Geotechnics,
693   113 (2019) 103088.

694 [40] C. Boon, G. Houlsby, S. Utili, A new contact detection algorithm for three-dimensional non-
695   spherical particles, Powder Technol., 248 (2013) 94-102.

696 [41] J. Eliáš, Simulation of railway ballast using crushable polyhedral particles, Powder Technol., 264
697   (2014) 458-465.

698 [42] C. Recarey, I. Pérez, R. Roselló, M. Muniz, E. Hernández, R. Giraldo, E. Oñate, Advances in
699   particle packing algorithms for generating the medium in the Discrete Element Method, Computer
700   Methods in Applied Mechanics and Engineering, 345 (2019) 336-362.

701 [43] S. Fortune, A sweepline algorithm for Voronoi diagrams, Algorithmica, 2 (1987) 153–174.

702 [44] J.A.R. Blais, M.A. Soofi, Spherical Harmonic Transforms Using Quadratures and Least Squares,
703   in: International Conference on Computational Science, 2006.

704 [45] E.J. Garboczi, Three-dimensional mathematical analysis of particle shape using X-ray tomography
705   and spherical harmonics: Application to aggregates used in concrete, Cement Concrete Research,
706   32 (2002) 1621-1638.

707 [46] D. Su, W.M.J.P.T. Yan, 3D characterization of general-shape sand particles using microfocus X-
708   ray computed tomography and spherical harmonic functions, and particle regeneration using
709   multivariate random vector, (2017).

710 [47] B. Zhou, J.J.I.J.f.N. Wang, A.M.i. Geomechanics, Generation of a realistic 3D sand assembly using
711   X-ray micro-computed tomography and spherical harmonic-based principal component analysis:
712   Generation of a Realistic 3D Sand Assembly, 41 (2017).

713 [48] D. Wei, J. Wang, N. Jiayan, B.J.C. Zhou, Geotechnics, Generation of realistic sand particles with
714   fractal nature using an improved spherical harmonic analysis, 104 (2018) 1-12.

715 [49] G. Mollon, J. Zhao, Fourier–Voronoi-based generation of realistic samples for discrete modelling
716   of granular materials, Granular Matter, 14 (2012) 621-638.

717 [50] P. Vangla, N. Roy, M.L.J.G.M. Gali, Image based shape characterization of granular materials and
718   its effect on kinematics of particle motion, 20 (2018) 6.

719 [51] Z. Nie, Z. Liang, X. Wang, A three-dimensional particle roundness evaluation method, 20 (2018)
720   32.

721 [52] D. Gross, M. Li, Constructing microstructures of poly- and nanocrystalline materials for numerical
722   modeling and simulation, Applied Physics Letters, 80 (2002) 746-748.

723 [53] J.F. Ferellec, G.R. Mcdowell, A method to model realistic particle shape and inertia in DEM,
724   Granular Matter, 12 (2010) 459-467.

725 [54] J.E. Andrade, K.-W. Lim, C.F. Avila, I. Vlahinić, Granular element method for computational
726   particle mechanics, Computer Methods in Applied Mechanics and Engineering, 241-244 (2012)

727   262-274.

728 [55] R. Kawamoto, E. Andò, G. Viggiani, J.E. Andrade, Level set discrete element method for three-
729   dimensional computations with triaxial case study, Computer Methods in Applied Mechanics and
730   Engineering, 91 (2016) 1-13.

731

732